Formation and decomposition of vacancy-rich clinopyroxene in a shocked eucrite: New insights for multiple impact events

Ai-Cheng Zhang [a, b,*], Jie-Ya Li [a], Jia-Ni Chen [a], Yuan-Yun Wen [c], Yan-Jun Guo [d], Yang Li [b, c], Naoya Sakamoto [e], and Hisayoshi Yurimoto [e, f]

[a] State Key Laboratory for Mineral Deposits Research, School of Earth Science and Engineering, Nanjing University, Nanjing 210023, China

[b] CAS Center for Excellence in Comparative Planetary, Hefei 230026, China

[c] Center for Lunar and Planetary Sciences, Institute of Geochemistry, Chinese Academy of Sciences, Guiyang 550081, China

[d] CAS Key Laboratory of Standardization and Measurement for Nanotechnology, CAS Center for Excellence in Nanoscience, National Center for Nanoscience and Technology, Beijing, China

[e] Isotope Imaging Laboratory, Creative Research Institution, Hokkaido University, Sapporo 010-0021, Japan

[f] Department of Natural History Sciences, Hokkaido University, Sapporo 060-0810, Japan

*Corresponding author. Ai-Cheng ZHANG (aczhang@nju.edu.cn)

For submission to ***Geochimica et Cosmochimica Acta***

Abstract

Impact is a fundamental process shaping the formation and evolution of planets and asteroids. It is inevitable that some materials on the surface of planets and asteroids have been impacted for many times. However, unambiguous petrological records for multiple post-formation impact events are rarely described. Here, we report that the thin shock melt veins of the shocked eucrite Northwest Africa 8647 are dominated by a fine-grained intergranular or vermicular pigeonite and anorthite assemblage, rather than compact vacancy-rich clinopyroxene. Vacancy-rich clinopyroxene in the veins instead is ubiquitous as irregularly-shaped, relict grains surrounded by intergranular or vermicular pigeonite and anorthite assemblage. The silica fragments entrained in shock melt veins contain a coesite core and a quartz rim. The occurrences of vacancy-rich clinopyroxene and coesite can be best explained by two impact events. The first impact event produced the shock melt veins and lead to the formation of vacancy-rich clinopyroxene and coesite. The second impact event heated the fine-grained melt veins and lead to the widespread partial decomposition of vacancy-rich clinopyroxene and the partial back-transformation of coesite. This paper is the first report of the decomposition reaction of shock-induced vacancy-rich clinopyroxene in extraterrestrial materials. We propose that widespread decomposition and/or back-transformation of high-pressure minerals in shocked meteorites can be considered as important records of multiple impact events.

1. Introduction

Impact is one of the most fundamental processes during the formation and evolution of the planets and their moons, and asteroids in the Solar System. Shock wave in impact events can cause a variety of physicochemical modifications in planetary materials, such as fragmentation, deformation, phase transformation, melting, and even vaporization. Impact conditions and the history of planetary materials can be constrained by studying the behaviors of minerals in shocked rocks. In the past several decades, abundant mineralogical and geochemical investigations based on shocked natural samples and laboratory-recovery samples have been performed for constraining shock conditions, such as shock pressure, post-shock temperature, post-shock thermal history, and dwell time (e.g., Sharp and DeCarli, 2006; Gillet and El Goresy, 2013; Fritz et al., 2017; Tomioka and Miyahara, 2017).

Surfaces of airless bodies are decorated by abundant impact craters of various scales from a few micrometers to thousands of kilometers in diameter, indicating their complex impact histories in the past 4.56 billion years (Melosh, 2011). It is inevitable that some rocks on the surface of airless bodies have experienced multiple post-formation impact events, which makes it very challenging to precisely unravel their thermal histories. A few geochronological investigations have suggested that some meteorites probably have experienced multiple impact events (e.g., Yin et al., 2014; Li and Hsu, 2018; Liao et al., 2019; Miyahara et al., 2021). However, unambiguous petrological records of multiple impact events, such as cross cutting relationships, where new shock melt veins cut old veins, are rarely reported. This scarcity is due to three aspects of facts. First, natural planetary materials are usually composed of various constituent minerals and have complex petrographic textures. As a consequence, various shock metamorphic records in a single shocked sample could be attributed to either highly heterogeneous responses in different regions or multiple impact events (e.g., El Goresy et al., 2013; Walton et al., 2014). Second, it is likely that second intense impact events may have completely erased the records that formed in first impact events. Third, shock metamorphic behaviors of natural minerals and rocks

are still far from well-understood compared with laboratory static and dynamic high-pressure experiments. Therefore, there are very few petrologic investigations inferring multiple impact events in meteorites (Miyahara et al., 2011; Friedrich et al., 2014). Miyahara et al. (2011) reported the presence of poorly-crystallized materials as inclusions in majorite grains from a L6 chondrite and suggested that the poorly-crystallized materials are vitrified (Mg,Fe)SiO_3-perovskite. They further proposed that the vitrified (Mg,Fe)SiO_3-perovskite and the host majorite formed in two different impact events, respectively (Miyahara et al., 2011). Friedrich et al. (2014) observed internally inconsistent petrofabrics among different lithologies in the Northwest Africa (NWA) 7298 H-group chondrite breccia. They interpreted that this feature could be a record of multiple impact events (Friedrich et al., 2014).

NWA 8647 is a brecciated eucrite, containing shock-induced melt veins with a large variation in width (Bouvier et al., 2017; Li et al., 2020). Li et al. (2020) described the petrography and mineralogy of NWA 8647 and discovered a corundum xenocryst included in pyroxene, suggesting that an Al-rich lithology existed in the interior of the eucrite parent body. During further studying this sample, we found that the vacancy-rich clinopyroxene grains in shock melt veins have been widely replaced by intergranular and vermicular pigeonite and anorthite assemblage. The silica fragments entrained in melt veins contain coesite cores and quartz rims. Here, we report the mineralogical features of materials in shock melt veins in this meteorite and suggest that the intergranular and vermicular pigeonite and anorthite assemblage are decomposition products of preexisting vacancy-rich clinopyroxene. The formation and decomposition of vacancy-rich clinopyroxene can best be explained by two distinct impact events. The formation of vacancy-rich clinopyroxene took place in the first impact event, and a subsequent impact event lead to its widespread decomposition.

2. Analytical methods

The polished section used in the present study and that used in Li et al. (2020) were prepared from a common chip of NWA 8647. Petrographic observations of the

eucrite NWA 8647 were carried out using the Zeiss Supra55 field emission scanning electron microscope (FE-SEM) under backscattering electron (BSE) mode at Nanjing University, Nanjing, China. The FE-SEM instrument was operated at an accelerating voltage of 15 kV. Chemical compositions of minerals larger than 2 μm were measured using the JEOL 8100 electron probe microanalyzer (EPMA) at Nanjing University. A 15-kV accelerating voltage and a 20-nA beam current were used for the EPMA analyses. Focused beams were used for most individual minerals (except for plagioclase) while defocused beams of 5-μm (in diameter) were used for measurements on plagioclase and fine-grained mineral assemblage in shock-induced melt veins. The counting times for element peaks and background are 20 s and 10 s, respectively. The detection limits are 0.02 wt% for SiO_2, 0.03 wt% for TiO_2, 0.02 wt% for Al_2O_3, 0.02 wt% for Cr_2O_3, 0.02 wt% for MgO, 0.02 wt% for FeO, 0.02 wt% for CaO, 0.02 wt% Na_2O, and 0.01 wt% for K_2O. Natural and synthetic standards were used for concentration calibration. All data were reduced with the atomic number-absorption-fluorescence (ZAF) procedure.

Structural characterization of minerals with grain size larger than 1 μm was performed using electron backscatter diffraction (EBSD) technique and Raman spectroscopy. The EBSD patterns of minerals were obtained using the JEOL 7000F FE-SEM instrument at Hokkaido University, Sapporo, Japan. The sample preparation and operation conditions for EBSD analyses are the same as those described in Li et al. (2020). During analysis, qualitative SEM-EDS compositions and EBSD patterns of certain target phases were obtained simultaneously. Then, the experimental EBSD patterns were indexed with potentially candidate phases in the databases. The Aztec software automatically suggests indexing solutions ranked by the number of indexed bands and the lowest “mean angular deviation” (MAD) values. The indexing with more well-indexed bands (usually 9 to 10 bands) and lower MAD values (<1) are considered desirable for an accurate solution. The Raman spectra of minerals were collected using the Renishaw in via Plus microRaman spectrometer with a charge couple device detector at the National Center for Nanoscience and Technology of China, Beijing. The exciting laser wavelength was 514 nm and the laser power on the sample with a spot

size of 1 μm was ~10 mW. The collection time for each spectrum was 60 s.

Three ultra-thin sections were prepared for transmission electron microscopic (TEM) observations in this study. The ultra-thin foils were cut using the FEI Scios SEM-focused ion beam (FIB) instrument at the Institute of Geochemistry, Chinese Academy of Sciences, Guiyang, China. The preparation procedure is the same as that described in Wang et al. (2019). The final thickness of the FIB sections is approximately 100 nm. The TEM observations were carried out using a FEI Tecnai F20 TEM instrument at Nanjing University. The accelerating voltage of the TEM instrument was 200 kV. The sections were studied at both Bright Field (BF) TEM mode and HAADF-STEM (High Angle Annual Dark Field-Scanning Transmission Electron Microscope) mode. Selected-area electron diffraction (SAED) and high-resolution TEM imaging were performed for structural indexing. Energy-dispersive X-ray spectroscopy (EDS) under TEM and STEM modes was used for qualitative to semiquantitative analyses of phases in the FIB sections.

3. Results

The polished section of NWA 8647 used in the present study contains a wide shock melt vein (6–8 mm in width) and several thin melt veins (a few micrometers to 900 μm in width; Fig. 1). The melted regions and the relict host rock have roughly equal proportions in the studied section. Fusion crust is absent in the sample used in this study. The host rock is composed mainly of moderate-coarse grained pyroxene with exsolution lamellae and anorthitic plagioclase. Minor phases in the host rock are silica phases (mainly amorphous silica with minor quartz, Fig. S1), ilmenite, chromite, troilite, merrillite, and zircon. Although NWA 8647 is a breccia, no fine-grained matrix typical of polymict eucritic breccias and howardites is present in the section used in the present study.

The wide melt vein is composed mainly of fine-grained (approximately 10–20 μm in size) pyroxene (mainly pigeonite with minor subcalcic augite) and plagioclase with a subophitic texture; the small pyroxene grains are usually chemically zoned with a

relatively dark core and a bright rim in BSE imaging. Relict lithic and mineral fragments are commonly observed in the wide melt vein (Fig. 1). Most of the thin melt veins and the wide melt vein show a roughly similar extension direction (Fig. 1). A few thin melt veins are connected with the wide melt vein. However, no thin melt veins cutting cross the wide melt vein were observed. The thin melt veins are composed of very fine-grained (mainly submicron in grain size) pigeonite and plagioclase, which mainly demonstrate an intergranular texture (Figs. 2a and 2b). The relative abundances of pigeonite and anorthite are not evenly distributed among different thin melt veins. A few mineral fragments (pyroxene, plagioclase, and silica phase) of tens of micrometers in dimension are present in these thin melt veins. In the thin melt veins connected with the wide melt vein, there is a transition from fine-grained subophitic texture to intergranular texture within a distance of 100–200 μm from the wide melt vein (Fig. S2).

In many of the thin melt veins, irregular vacancy-rich clinopyroxene grains of submicron to a few micrometers in size are observed but have a low abundance (Figs. 2b–2f). In BSE images, the vacancy-rich clinopyroxene grains have an intermediate Z-contrast between pigeonite and anorthite in the fine-grained matrix and usually have a brighter pigeonite overgrowth (Fig. S3a). The vacancy-rich clinopyroxene grains are locally abundant in volume in a few thin melt veins (Figs. 2c–2f), which appear spatially closer to the wide melt vein than those with low abundance of vacancy-rich clinopyroxene. Most of the vacancy-rich clinopyroxene grains have been partly replaced by a very fine-grained, vermicular assemblage of pigeonite and anorthite along the grain rims (Figs. 2c–2f). Some of the vermicular fine-grained assemblage appears as a pseudomorph of their precursor grains (Figs. 2d, 2f, and S4). It is noteworthy that no spatially preferred locations were observed for the enrichment of vacancy-rich clinopyroxene in the thin melt veins (<1 mm).

The vacancy-rich clinopyroxene has a large chemical variation among different grains and contains high concentrations of cation vacancy (23–30 mol% Ca-Eskola component $(Ca_{0.5}\square_{0.5})AlSi_2O_6$; Table 1). Their compositional range is roughly

comparable to that of the fine-grained mineral assemblage as determined by defocused beam analysis using a spot size of 5 μm in diameter (Table 2; Fig. S5). The EBSD patterns of vacancy-rich clinopyroxene phase were indexed with different structures of pyroxene, garnet, and other silicate phases containing Ca, Al, Mg, and Fe in the databases installed in the Aztec software. Only the *C2/c* augite structure can index the EBSD patterns with MAD values less than 1, indicating the vacancy-rich clinopyroxene has the *C2/c* augite structure (Fig. 3). A FIB section containing both the vacancy-rich clinopyroxene and the surrounding vermicular mineral assemblage was prepared for TEM observations (Fig. 4a). Under BF-TEM mode, the vacancy-rich clinopyroxene shows a mottled texture (Fig. 4b) and resulting SAED patterns can only be indexed with the *C2/c* augite crystal structure (Fig. 4c), consistent with the EBSD results. The TEM-EDS measurements show that the pigeonite grains in the fine-grained mineral assemblage have CaO and Al_2O_3 contents much lower than the vacancy-rich clinopyroxene (Fig. S6), consistent with the elemental mapping results (Fig. S7). Their SAED patterns are best indexed with the $P2_1/c$ pigeonite crystal structure (Fig. 4d). No mottled texture was observed in the pigeonite grains (Fig. 4b). The anorthite phase in the fine-grained mineral assemblage is identified based on its high-resolution TEM images and Fast Fourier Transfer patterns (Fig. S8).

The pyroxene fragments entrained in the thin melt veins are low-pressure phases, and no high-pressure polymorphs such as akimotoite and majorite were identified. The Si,Al,Ca-regions (interpreted as original plagioclase fragments) show no sharp boundaries with surrounding fine-grained matrix (Figs. 5a–5c). In BSE images, kyanite grains are occasionally observed as slightly brighter, acicular crystals in the Si,Al,Ca-regions (Figs. 5a–5c). A few irregular grossular grains were also identified in the kyanite-bearing regions based on their qualitative STEM-EDS features (Fig. S9) and SAED patterns (Fig. S10). No silica high-pressure polymorphs were observed in the kyanite-bearing regions. The silica fragments entrained in the thin melt veins usually have a coesite core surrounded by a 2–20 μm quartz margin (Figs. 6a–6b, S11, and S12). In some silica fragments, the margin also contains small coesite grains (Fig. 6b).

The core-margin texture is also present in the silica fragments entrained in the wide shock melt vein. One FIB section (Fig. 6b) was prepared from a silica fragment entrained in a thin melt vein. The BF-TEM observations show that the coesite core is an aggregate of lath-shaped coesite grains with twinning structure rather than a single crystal (Fig. 6c). However, no twinning structure was observed for the small coesite grains at the margin of the silica fragments (Figs. 6c and 6d).

4. Discussion

4.1. Formation and decomposition of vacancy-rich clinopyroxene

Vacancy-rich clinopyroxene (Ca-Eskola type pyroxene) has been reported in both terrestrial and extraterrestrial rocks, and static high-pressure experimental run products. In terrestrial rocks, vacancy-rich clinopyroxene is present in omphacites and mantle-derived eclogites (e.g., Vogel, 1966; Essene and Fyfe, 1967; Harte and Gurney, 1975; Smyth, 1980; Anderson and Moecher, 2007; Heidelbach and Terry, 2013). In extraterrestrial rocks, vacancy-rich clinopyroxene has usually been observed as tissintite or Mg,Fe-rich tissintite in shock melt veins, reported from numerous shocked meteorites (e.g., Walton et al., 2014; Ma et al., 2015; Pang et al., 2016; Ma and Beckett, 2017; Chen et al., 2019; Sharp et al., 2019; Zhang et al., 2021). Static high-pressure experimental results suggest that the Ca-Eskola type vacancy occurs at high pressures, probably higher than 3 GPa (Smyth, 1980; Konzett et al., 2008; Zhao et al., 2011). In a recent static high-pressure experimental study, tissintite has been synthesized from crystalline and amorphous plagioclase at pressures ranging from 6 to 8.5 GPa and temperatures of 1000–1300 ^{o}C (Rucks et al., 2018). The vacancy-rich clinopyroxene in NWA 8647 is also Ca-Eskola type, and only observed in the thin melt veins. The restricted occurrence of vacancy-rich clinopyroxene points to a high-pressure origin, based on the observations of Ca-Eskola-type pyroxene in terrestrial and extraterrestrial rocks (Vogel, 1966; Essene and Fyfe, 1967; Harte and Gurney, 1975; Smyth, 1980; Anderson and Moecher, 2007; Heidelbach and Terry, 2013; Walton et al., 2014; Ma et al., 2015; Pang et al., 2016; Ma and Beckett, 2017; Chen et al., 2019; Sharp et al., 2019; Zhang et al., 2021). Additionally, coesite and kyanite-grossular are

observed in the silica and plagioclase fragments, respectively, entrained in the thin melt veins containing vacancy-rich clinopyroxene. The appearance that the coesite core is a polycrystalline aggregate of twinned coesite grains suggests that coesite may have formed by crystallization from an undercooled high-pressure silica melt (Langenhorst, 2003). The kyanite-grossular assemblage has been reported in the shocked eucrite NWA 2650, in which kyanite-grossular-silica crystallized from a melted plagioclase entrained in a shock melt vein (Chen et al., 2019). Although no silica phase closely associated with kyanite-grossular is observed in the present study, we suspect that the formation of the kyanite-grossular assemblage in the present study is also related to decomposition of anorthite at high pressures, probably during shock-induced melting of plagioclase. Therefore, the coexistence of kyanite and grossular in thin melt veins supports the high-pressure origin of vacancy-rich clinopyroxene, as suggested above.

Formation conditions of the high-pressure minerals in NWA 8647 can be constrained based on mineral stability fields determined from static high-pressure experiments. The stability field of vacancy-rich clinopyroxene chemically similar to the present study has not yet been experimentally determined. Using omphacite as an analog (Liu, 1980), the Na-poor, vacancy-rich clinopyroxene has a broad stability pressure, probably larger than 2 GPa and even up to 20 GPa. Static high-pressure experimental results suggested that the Ca-Eskola type vacancy occurs at high pressures, probably higher than 3 GPa (Smyth, 1980; Konzett et al., 2008; Zhao et al., 2011). Coesite can form at a pressure range of 2.5–13 GPa in static high-pressure experiments (Zhang et al., 1996). In many shocked meteorites containing silica phases (e.g., Miyahara et al., 2014; Pang et al., 2016; Chen et al., 2019), stishovite and coesite often coexist with each other. However, in the present study, coesite is widely present in melt veins, but stishovite is absent. This observation may imply that the pressure did not exceed 8 GPa or the temperature was too high to stabilize stishovite (De Carli and Milton, 1965; Mansfeld et al., 2017). Considering the large kinetic barrier for phase transformation from low-pressure silica phase to coesite (Perrillat et al., 2003), high temperatures are required to reduce the kinetic effect during the formation of coesite.

Therefore, the absence of stishovite in this study may be due to high temperatures in the melt veins, although a limited shock pressure cannot be excluded.

According to the high-pressure and high-temperature phase diagram of anorthite (Liu et al., 2012), the kyanite-grossular assemblage occurs at pressures between ~2.5 GPa and ~15 GPa. The absence of silica phase in the kyanite-grossular-bearing regions may be due to locally high temperatures (1400–2000 ^{o}C; Liu et al., 2012). Combining the above considerations together, we infer that the formation pressure for the high-pressure minerals in the thin melt veins of NWA 8647 was between 3 and 13 GPa and the temperature in the shock melt veins was up to 1400–2000 ^{o}C. However, a higher transient peak shock pressure is possible, considering many high-pressure minerals in shocked meteorites form during decompression (Fritz et al., 2017).

The petrographic texture of vacancy-rich clinopyroxene in NWA 8647 is different from that observed in other shocked meteorites in the literature (e.g., Walton et al., 2014; Ma et al., 2015; Pang et al., 2016; Ma and Beckett, 2017; Chen et al., 2019; Sharp et al., 2019; Zhang et al., 2021). The vacancy-rich clinopyroxene previously described in shocked meteorites (especially HED meteorites) usually occurs as compact grains in shock melt veins or at the margin of zoned melt veins (Pang et al., 2016; Chen et al., 2019). However, the vacancy-rich clinopyroxene grains in NWA 8647 are surrounded by fine-grained, intergranular or vermicular pigeonite and anorthite (Figs. 2 and S3). It is reasonable to assume that the thin melt veins in NWA 8647 were originally dominated by compact vacancy-rich clinopyroxene grains, similar to those in other shocked eucrites (e.g., Pang et al., 2016; Chen et al., 2019). If this assumption is correct, the observed vermicular and intergranular pigeonite and anorthite assemblage must represent a secondary texture after the formation of vacancy-rich clinopyroxene and can be best attributed to the decomposition reaction of vacancy-rich clinopyroxene. This inference is supported by two other aspects of consideration. First, high-pressure minerals become unstable or metastable at ambient pressure-temperature conditions. Especially, the high cation vacancy (23–30 mol% Ca-Eskoka) is unfavorable for the stability of clinopyroxene at low pressures (Smyth, 1980). Therefore, phase transformation from vacancy-rich clinopyroxene to its low-pressure phase or mineral

assemblage may take place either spontaneously or when later thermal events occurred. Similar vermicular textures have been observed for the vacancy-rich omphacite grains in retrograded eclogites or kimberlites and had been attributed to the decomposition of vacancy-rich omphacite (e.g., Smyth, 1980; Anderson and Moecher, 2007; Heidelbach and Terry, 2013). However, the presence of relict vacancy-rich clinopyroxene may exclude the possibility that the decomposition to vermicular and intergranular pigeonite and anorthite assemblage is spontaneous. Otherwise, no relict vacancy-rich clinopyroxene would be observed in this study and in other shocked eucrites containing vacancy-rich clinopyroxene (e.g., Pang et al., 2016; Chen et al., 2019). Instead, a post-formation thermal event is required for the decomposition of vacancy-rich clinopyroxene and will be discussed in the following section. Second, the vacancy-rich clinopyroxene grains are roughly comparable in chemical compositions with the vermicular and intergranular mineral assemblages (Fig. S5), supporting the interpretation involving the decomposition.

4.2. Constraints for multiple impact events

The decomposition of vacancy-rich clinopyroxene indicates that a post-formation thermal event caused the back-transformation of early-formed high-pressure minerals. In NWA 8647, the unique texture of most silica fragments in shock melt veins (i.e., coesite cores with quartz rims) also supports this inference. It is well known that the transformation from low-pressure silica phases to coesite has a large kinetic barrier (Miyahara et al., 2014 and references therein). Therefore, it would be expected that in shocked meteorites the transformation to coesite in the silica fragments proceeds inward from the interface with surrounding shock melt following the temperature gradient in the silica fragments (hotter at the rim and colder at the interior). This expectation is supported by the observations that coesite grains usually occur at the margin of the silica fragments in shock melt veins reported in the literature (e.g., Figs. 3c and 3d of Pang et al., 2016; Fig. 5 of Chen et al., 2019). However, this documented occurrence of coesite-rimmed clasts is contrary to our observation of coesite in NWA 8647, which are typically mantled by quartz grains. A reasonable explanation is that originally the silica fragments had largely or even totally transformed into coesite

aggregates during the formation of shock melt veins. A subsequent thermal event only affected the margins of early-formed coesite aggregates and caused their back-transformation into quartz at the margins. This explanation is consistent with the absence of twinning structure in the coesite grains at the margin, which can be explained as a product of thermal annealing at the margins of silica fragments (Fig. 6c).

Back-transformation of high-pressure minerals in meteorites has been reported in the literature (Chen et al., 1998; Kimura et al., 2003; Walton, 2013; Bzhan et al., 2017; Hu et al., 2017; Fukimoto et al., 2020; Miyahara et al., 2021), although the decomposition of shock-induced vacancy-rich clinopyroxene is observed for the first time in the present study. For NWA 8647, four processes may provide the potential heat for the decomposition of vacancy-rich clinopyroxene and the back-transformation of coesite: (1) thermal metamorphism on the eucrite parent body; (2) aerodynamic heating during atmospheric passage; (3) post-shock annealing; and (4) another impact event.

Thermal metamorphism usually involves high temperature but low pressure and is an important process in the early history of the eucrite parent body (Yamaguchi et al., 1996). However, thermal metamorphism is a long-term process, probably at a temporal scale of million years on the eucrite parent body (Yamaguchi et al., 1997). Although a thermal metamorphic event of such a long duration could explain the decomposition of vacancy-rich clinopyroxene and the back-transformation of coesite to quartz, a coarsened texture would be expected for the shock melt veins and the chemical zoning of pyroxene in the melted region would be erased. In addition, the decomposition products of vacancy-rich clinopyroxene are expected to have comparable grain sizes in different regions throughout the whole meteorite. These inferences are in conflict with the petrographic observations in the present study. The spatial scale of thermal metamorphism should be much larger than the meteorite scale. For example, it is difficult to interpret the heterogeneous distribution of twinning structure in coesite grains with a distance of a few micrometers (Fig. 6). Thus, the decomposition of vacancy-rich clinopyroxene and the back-transformation of coesite cannot be explained by the thermal metamorphic events on the eucrite parent

364 body. Instead, it is more likely that a short-term heating event induced the
365 decomposition and back-transformation.

366 Aerodynamic heating during atmospheric passage has been used to explain the
367 back-transformation of high-pressure minerals near the fusion crust of an H6 ordinary
368 chondrite (Kimura et al., 2003; Fukimoto et al., 2020). Based on the observations in
369 Kimura et al. (2003) and Fukimoto et al. (2020), the aerodynamical heating only
370 affected a distance of approximately 300 μm from the fusion crust and the high-
371 pressure minerals further away from the fusion crust may retain their high-pressure
372 structures. However, in NWA 8647, the decomposition of vacancy-rich clinopyroxene
373 is widely observed at a scale of at least centimeters and no fusion crust is present in
374 the studied sections. Therefore, aerodynamic heating during atmospheric passage can
375 be excluded as the driving force for the decomposition of vacancy-rich clinopyroxene
376 and the back-transformation of coesite in NWA 8647.

377 Post-shock annealing has been proposed to explain the back-transformation of
378 high-pressure minerals in shocked meteorites (e.g., Chen et al., 1998; Walton, 2013;
379 Bazhan et al., 2017; Hu and Sharp, 2017; Miyahara et al., 2021). Whether back-
380 transformation takes place in shock melt veins depends on the peak temperatures and
381 cooling rates of the regions in shock melt veins. Low peak temperatures and fast
382 cooling rates prevent high-pressure minerals from back-transformation. Hu and Sharp
383 (2017) performed thermal modeling of shock melts of 0.8 mm and 1.0 mm in thickness
384 and entrained clasts to evaluate the cooling rates of various regions in and adjacent to
385 the shock melt veins. The authors concluded that thicker melt veins lead to slower
386 cooling and extensive back-transformation after shock-pressure release. Meanwhile,
387 the major part of the melt vein with a short distance from the cold host would have a
388 higher cooling rate than the vein interior and the high-pressure minerals therein may
389 survive (Hu and Sharp, 2017). The thin shock melt veins in NWA 8647 have a variation
390 in width from several micrometers to tens of micrometers to 0.9 mm. Through
391 comparison of the widths of the thin shock melt veins in NWA 8647 with the thermal
392 models in Hu and Sharp (2017), most of the thin veins should still retain the high-
393 pressure minerals (presumably vacancy-rich clinopyroxene). Shaw and Walton (2013)

394 modeled the cooling times of shock melts in Martian meteorites and considered the
395 spatial distribution of shock melts. They found that interference between thermal
396 haloes of closely spaced shock melts may extend cooling times by a factor of 1.4 to
397 100 (hottest part). The overlapping effect of thermal haloes may be significant in the
398 section used in the present study, considering the presence of the wide melt vein (6–
399 8 mm wide). The finer subophitic texture of a thin melt vein (shown in Fig. S2) near
400 the wide melt vein may be explained by this effect. However, the extended cooling
401 times cannot account for at least three aspects of observations in the present study.
402 First, the presence of vacancy-rich clinopyroxene at the center of some relatively thick
403 melt veins (up to hundreds of micrometers in width) indicates that the dwell time of
404 high pressure was not very short. Based on the consideration in Shaw and Walton
405 (2013), the very thin melt veins (e.g., ~15 μm in width shown in Fig. 2a) would still
406 have quenched rapidly and their crystallization would not have been largely affected
407 by the overlapping thermal effect. However, the observations indicate that the very
408 thin melt veins are also dominated by intergranular pigeonite-plagioclase assemblage,
409 which is not significantly different from those in relatively thick melt veins. Second,
410 since the host rock is originally cold, the cooling rates in relatively thick, hot melt veins
411 (1400–2000 ^{o}C based on the presence of kyanite and grossular) would be zoned, with
412 rapidly cooled vein edges and slowly cooled vein centers. Considering the overlapping
413 thermal effect, we would expect the cooling rate at the vein centers to be slower.
414 Vacancy-rich clinopyroxene grains at the vein centers would have a longer time to
415 decompose into pigeonite and anorthite than those at the vein edges. As a
416 consequence, vacancy-rich clinopyroxene grains would be more largely retained at the
417 vein edges than at the vein centers. However, no such spatial regularity was observed
418 for the relict vacancy-rich clinopyroxene grains in NWA 8647, even in the relatively
419 thick melt veins. Third, the post-shock annealing models in Hu and Sharp (2017) and
420 Shaw and Walton (2013) involve thermal diffusions at a scale of millimeters to
421 centimeters. If most of the thin melt veins have been experienced the post-formation
422 annealing, it is very difficult to explain the heterogeneous distribution of twinning in
423 coesite grains at a scale of micrometers and the abundant strains in vacancy-rich

clinopyroxene as revealed by its mottled texture at a scale of nanometers. Recently, Miyahara et al. (2021) studied the high-pressure minerals in the shocked eucrite Padvarninkai, which contains a large area of shock melt veins (Fig. 1 of Miyahara et al., 2021) comparable to that in NWA 8647. In this meteorite, high-pressure minerals are present in the regions adjacent to the thin shock melt veins, but absent in the wide shock melt veins (>2 mm). The authors suggested that some tissintite aggregates and coesite in this meteorite underwent a back-transformation to amorphous (or anorthite) and quartz, respectively (Miyahara et al., 2021). However, most of the high-pressure minerals (tissintite and garnet) in Padvarninkai remain unchanged (Miyahara et al., 2021). This feature is also distinctly different from the observations in NWA 8647. Therefore, it is difficult to explain the widespread decomposition texture of vacancy-rich clinopyroxene in thin melt veins from NWA 8647 with the post-shock annealing model.

A second impact event is the most likely explanation for the decomposition of vacancy-rich clinopyroxene and back-transformation of coesite in NWA 8647. Studies of shocked rocks from terrestrial impact structures and numerical models demonstrate that shock-induced temperature rise is highly heterogeneous and intense shock wave interferences at interfaces and grain boundaries may lead to a large temperature rise there (Sharp and DeCarli, 2006; Fritz et al., 2017). With this behavior of shock wave in mind, shock-induced heating can readily account for the decomposition of vacancy-rich clinopyroxene and the back-transformation of coesite along grain boundaries and the interfaces between different phases, respectively, in NWA 8647. The shock-induced heating along interfaces can also explain why the relict coesite grains at the margin of silica fragments contain no twinning structure but the (cold) interior coesite grains show widespread twinning. Since originally composed of fine-grained minerals (presumably micrometer-sized vacancy-rich clinopyroxene), the melt veins are the locations where the temperature was readily raised compared with the coarse-grained host rock. Consequently, abundant vacancy-rich clinopyroxene grains decomposed into fine-grained pigeonite and anorthite assemblage during the second impact event. It is likely that some regions may also have melted and recrystallized in the second

impact event, with some pigeonite grains nucleated and overgrown on the relict vacancy-rich clinopyroxene. Given the spatial relationship between the thin melt veins and the wide melt vein, it follows that the simplest explanation is that the wide melt vein formed in the second impact event. The heating from the second impact event - and the heat retention and slower cooling associated with it - is consistent with the large width of the wide vein, and led to the lack of preservation of high-pressure phases.

The NWA 8647 meteorite is classified as a brecciated eucrite based solely on the presence of basaltic lithologies and mineral fragments set into a fine-grained melt-rich matrix (Bouvier et al., 2017). However, no detailed information about the basaltic lithologies was reported in the Meteoritical Bulletin description. Based on the observations in Li et al. (2020) and the present study, no typically fine-grained matrix and exotic materials are present in NWA 8647. This feature indicates that NWA 8647 is a monomict, fragmental breccia. A schematic diagram of the impact history of NWA 8647 is shown in Fig. 7. Fragmentation of the source rock of NWA 8647 and mixing of the fragments with various grain sizes should have taken place prior to the formation of thin shock melt veins with their vacancy-rich clinopyroxene. Then, a subsequent impact event caused the partial decomposition of vacancy-rich clinopyroxene and back-transformation of coesite, and the formation of the wide melt vein.

Two types of petrological records have been used to infer multiple impact events in the literature (e.g., Miyahara et al., 2011; Friedrich et al., 2014). Miyahara et al. (2011) draw their conclusion based on the opposite-from-expected crystallization sequences for poorly-crystallized $(Mg,Fe)SiO_3$ material [presumably $(Mg,Fe)SiO_3$-perovskite] and majorite in between the shocked chondrite and the melting experiments. Friedrich et al. (2014) discriminated multiple impact events in a brecciated H chondrite NWA 7298 based on the inconsistent petrofabrics among three different lithologies. In contrast, the present study proposes that the formation and decomposition of vacancy-rich clinopyroxene and the back-transformation of coesite in NWA 8647 are best explained by two impact events. If this is correct, widespread

decomposition or back-transformation of high-pressure minerals may be used as a new indicator of unraveling multiple impact events in other shocked meteorites.

5. Conclusions

In this paper, we report the mineralogical features of shock melt veins in the eucrite NWA 8647. The thin melt veins (<1 mm in width) are dominated by abundant fine-grained intergranular pigeonite and anorthite. In many of these thin melt veins, vacancy-rich clinopyroxene is widely present as irregularly-shaped grains, but has a low abundance. Some of the vacancy-rich clinopyroxene grains are replaced by vermicular pigeonite and anorthite assemblage. Silica aggregates with a coesite core and a quartz rim are commonly observed in the melt veins. Some of the anorthitic plagioclase grains entrained in the melt veins contain submicron kyanite and grossular grains. The TEM observations reveal that the vacancy-rich clinopyroxene and coesite at the core of silica aggregates contain internal strains and twinning structure, respectively. However, the pigeonite grains and the coesite grains at the margin of silica aggregates lack internal strains and twinning structure, respectively. We suggest that the intergranular and vermicular assemblage of pigeonite and anorthite is a decomposition product of vacancy-rich clinopyroxene. The quartz grains surrounding coesite are the back-transformation product of coesite. The mineralogical features of thin melt veins, especially the widespread decomposition of vacancy-rich clinopyroxene, indicate that the eucrite NWA 8647 recorded multiple impact events.

Declaration of Competing Interest

The authors declare that they have no known competing financial interests or personal relationships that could have appeared to influence the work reported in this paper.

Acknowledgements

We appreciate the helpful comments from three anonymous reviewers and the editorial efforts from Associate Editor Christopher Herd and Executive Editor Jeffrey G.

Catalano. This work was financially supported by National Natural Science Foundation of China (42025302, 41673068, 41973061), the B-type Strategic Priority Program of the Chinese Academy of Sciences (XDB41000000), the pre-research Project on Civil Aerospace Technologies funded by CNSA (D020204).

References

Anderson E. D. and Moecher D. P. (2007) Omphacite breakdown reactions and relation to eclogite exhumation rates. *Contrib Mineral Petrol* **154**, 253–277.

Bazhan I. S., Litasov K. D., Ohtani E. and Ozawa, S. (2017) Majorite-olivine-high-Ca pyroxene assemblage in the shock-melt veins of Pervomaisky chondrite. *American Mineralogist* **102**, 1279–1286.

Bouvier A., Gattacceca J., Agee C., Grossman J. and Metzler, K. (2017) The Meteoritical Bulletin, No. 104. *Meteoritics and Planetary Science*. doi: 10.1111/ maps.12930.

Chen D. L., Zhang A. C., Pang R. L., Chen J. N. and Li Y. (2019) Shock-induced phase transformation of anorthitic plagioclase in the eucrite meteorite Northwest Africa 2650. *Meteoritics & Planetary Science* **54**, 1548–1562.

Chen M., Xie X., El Goresy A., Wopenka B. and Sharp, T. (1998) Cooling rates in the shock veins of chondrites: constraints on the $(Mg,Fe)_2SiO_4$ polymorph transformations. *Science in China (Series D)* **41**, 522–528.

De Carli P. S. and Milton D. J. (1965) Stishovite: synthesis by shock wave. *Science* **147**(3654), 144–145.

El Goresy A., Gillet Ph., Miyahara M., Ohtani E., Ozawa S., Lin Y., Feng L. and Escerig, S. (2013) Multiple impact events and diamond formation on Mars. *44th Lunar and Planetary Science Conference*. Abstract #1037.

Essene E. and Fyfe W. S. (1967) Omphacite in Californian metamorphic rocks. *Contrib Mineral Petrol*, **15**, 1–23.

Fukimoto K., Miyahara M., Sakai T., Ohfuji H., Tomioka N., Kodama Y., Ohtani E. and Yamaguchi A. (2020) Back-transformation mechanisms of ringwoodite and majorite in an ordinary chondrite. *Meteoritics & Planetary Science* **55**, 1749–1763.

Friedrich J. M., Weisberg M. K. and Rivers M. L. (2014) Multiple impact events recorded in the NWA 7298 H chondrite breccia and the dynamical evolution of an ordinary chondrite asteroid. *Earth and Planetary Science Letters* **394**, 13–19.

Fritz J., Greshake A. and Fernandes V. A. (2017) Revising the shock classification of meteorites. *Meteoritics & Planetary Science* **52**(6), 1216–1232.

Gillet P. and El Goresy A. (2013) Shock events in the Solar System: The message from minerals in terrestrial planets and asteroids. *Annual Review of Earth and Planetary Sciences* **41**, 257–285.

Harte B. and Gurney J. J. (1975) Evolution of clinopyroxene and garnet in an eclogite nodule from the Roberts Victors kimberlite pipe, South Africa. *Physics and Chemistry of the Earth* **9**, 367–387.

Heidelbach F. and Terry M. P. (2013) Inherited fabric in an omphacite symplectite: reconstruction of plastic deformation under high-pressure conditions. *Microscopy and Microanalysis* **19**, 942–949.

Hu J. and Sharp T. G. (2017) Back-transformation of high- pressure minerals in shocked chondrites: Low-pressure mineral evidence for strong shock. *Geochimica et Cosmochimica Acta* **215**, 277–294.

Kimura M., Chen M., Yoshida Y., El Goresy A. and Ohtani E. (2003) Back-transformation of high-pressure phases in a shock melt vein of an H-chondrite during atmospheric passage: Implications for the survival of high-pressure phases after decompression. *Earth and Planetary Science Letters* **217**, 141–150.

Konzett J., Frost D. J., Proyer A. and Ulmer P. (2008) The Ca-Eskola component in eclogitic clinopyroxene as a function pressure, temperature and bulk composition: an experimental study to 15 GPa with possible implications for the formation of orientated SiO_2-inclusions in omphacite. *Contrib Mineral Petrol* **155**, 215–228.

Langenhorst F. (2003) Nanostructures in ultrahigh-pressure metamorphic coesite and diamond: A genetic fingerprint. Mitteilungen der Österreichischen Mineralogischen Gesellschaft **148**, 401–412.

Li J. Y., Zhang A. C., Sakamoto N., Yurimoto H. and Gu L. X. (2020) A new occurrences of corundum in eucrite and its significance. *American Mineralogist* **105**, 1656–1661.

Li Y. and Hsu W. (2018) Multiple impact events on the L-chondritic parent body: Insights from SIMS U-Pb dating of Ca-phosphates in the NWA 7251 L-melt breccia. *Meteoritics & Planetary Science* **53**, 1081–1095.

Liu L. (1980) Phase relations in the system diopside-jadeite at high pressures and high temperatures. *Earth and Planetary Science Letters* **47**, 398–402.

Liu X., Ohfuji H., Nishiyama N., He Q., Sanehira T. and Irifune T. (2012) High-P behavior of anorthite composition and some phase relations of the CaO-Al_2O_3-SiO_2 system to the lower mantle of the Earth, and their geophysical implications. *Journal of Geophysical Research* **117**, B09205. DOI: 10.1029/2012JB009290

Liao S. Y., Hsu W. B., Wang Y., Li Y., Tang C. P. and Mei B. (2019) In situ Pb-Pb dating of silica-rich Northwest Africa (NWA) 6594 basaltic eucrite and its constraint on

thermal history of the Vestan crust. *Meteoritics & Planetary Science* **54**, 3064–3081.

Ma C., Tschauner O., Beckett J. R., Liu Y., Rossman G. R., Zhuravlev K., Prakapenka V., Dera P. and Taylor L. A. (2015) Tissintite (Ca,Na,□)$AlSi_2O_6$, a highly-defective, shock-induced, high-pressure clinopyroxene in the Tissint Martian meteorite. *Earth and Planetary Science Letters* **422**, 194–205.

Ma C. and Beckett J. R. (2017) A new type of tissintite, (Ca,Mg,Na,$□_{0.14}$)(Al,Fe,Mg)Si_2O_6, in the Zagami martian meteorite: a high-pressure clinopyroxene formed by shock. Lunar and Planetary Science XLVII. Abstract #1639.

Melosh H. J. (2011) Planetary surface processes. Cambridge University Press, New York.

Miyahara M., Ohtani E., Kimura M., Ozawa S., Nagase T., Nishijima M. and Hiraga K. (2011) Evidence for multiple dynamic events and subsequent decompression stage recorded in a shock vein. *Earth and Planetary Science Letters* **307**, 361–368.

Miyahara M., Yamaguchi A., Ohtani E., Tomioka N. and Kodama Y. (2021) Complicated pressure-temperature path recorded in the eucrite Padvarninkai. *Meteoritics & Planetary Science* **56**, 1443–1458.

Miyahara M., Ohtani E., Yamaguchi A., Ozawa S., Sakai T. and Hirao N. (2014) Discovery of coesite and stishovite in eucrite. *Proceedings of the National Academy of Sciences of the United States of America* **111**, 10939–10942.

Pang R. L., Zhang A. C., Wang S. Z., Wang R. C. and Yurimoto H. (2016) High-pressure minerals in eucrite suggest a small source crater on Vesta. *Scientific Reports* **6**, 26063.

Perrillat J. P., Daniel I., Lardeaux J. M. and Cardon H. (2003) Kinetics of the coesite-quartz transition: Application to the exhumation of ultrahigh-pressure rocks. *Journal of Petrology* **44**, 773–788.

Sharp T. G. and DeCarli P. S. (2006) Shock effects in meteorites. In *Meteorites and the Early Solar System II* (eds. D. S. Lauretta and H. Y. McSween). University of Arizona Press, Tuscon, pp. 653–677.

Sharp T. G., Walton E. L., Hu J. and Agee C. (2019) Shock conditions recorded in NWA 8159 Martian augite basalt with implications for the impact cratering history on Mars. *Geochimica et Cosmochimica Acta* **246**, 197–212.

Shaw C. S. J. and Walton E. L. (2013) Thermal modeling of shock melts in meteorites: Implications for preserving Martian atmospheric signatures and crystallization of high-pressure minerals from shock melts. Meteoritics and Planetary Science **48**, 758–770.

Smyth J. R. (1980) Cation vacancies and the crystal chemistry of breakdown reactions in kimberlitic omphacites. *American Mineralogist* **65**, 1185–1191.

617 Tomioka N. and Miyahara M. (2017) High-pressure minerals in shocked meteorites.
618 *Meteoritics & Planetary Sciences* **52**, 2017–2039.
619 Vogel D. E. (1966) Nature and chemistry of the formation of clinopyroxene-plagioclase
620 symplectite from omphacite. *Neues Jahrb Mineral Monatsh* **6**, 185–189.
621 Walton E. L. (2013) Shock metamorphism of Elephant Moraine A79001: Implications
622 for olivine-ringwoodite transformation and the complex thermal history of
623 heavily shocked Martian meteorites. *Geochimica et Cosmochimica Acta* **107**, 299–
624 315.
625 Walton E. L., Sharp T. G., Hu J. and Filiberto J. (2014) Heterogeneous mineral
626 assemblages in martian meteorite Tissint as a result of a recent small impact
627 event on Mars. *Geochimica et Cosmochimica Acta* **140**, 334–348.
628 Yamaguchi A., Taylor G. J. and Keil K. (1996) Global crustal metamorphism of the
629 eucrite parent body. *Icarus* **124**, 97–112.
630 Yamaguchi A., Taylor G. J. and Keil K. (1997) Metamorphic history of the eucritic crust
631 of 4 Vesta. *Journal of Geophysical Research* **102**(E6), 13381–13386.
632 Yin Q. Z., Zhou Q., Li Q. L., Li X. H., Liu Y., Tang G. Q., Krot A. N. and Jenniskens P. (2014)
633 Records of the Moon-forming impact and the 470 Ma disruption of the L
634 chondrite parent body in the asteroid belt from U-Pb apatite ages of Novato (L6).
635 *Meteoritics & Planetary Science* **49**, 1426–1439.
636 Zhang A. C., Jiang Q. T., Tomioka N., Guo Y. J., Chen J. N., Li Y., Sakamoto N. and Yurimoto,
637 H. (2021) Widespread tissintite in strongly shock-lithified lunar regolith
638 breccias. *Geophysical Research Letters* **48**, e2020GL091554.
639 Zhang J., Li B., Utsumi W. and Liebermann R. C. (1996) In situ X-ray observations of the
640 coesite-stishovite transition: Reversed phase boundary and kinetics. *Physics and*
641 *Chemistry of Minerals* **23**, 1–10.
642 Zhao S. T., Nee P., Green H. W. and Dobrzhinetskaya L. F. (2011) Ca-Eskola component
643 in clinopyroxene: Experimental studies at high pressures and high temperatures
644 in multianvil apparatus. *Earth and Science Research Letters* **307**, 517–524.

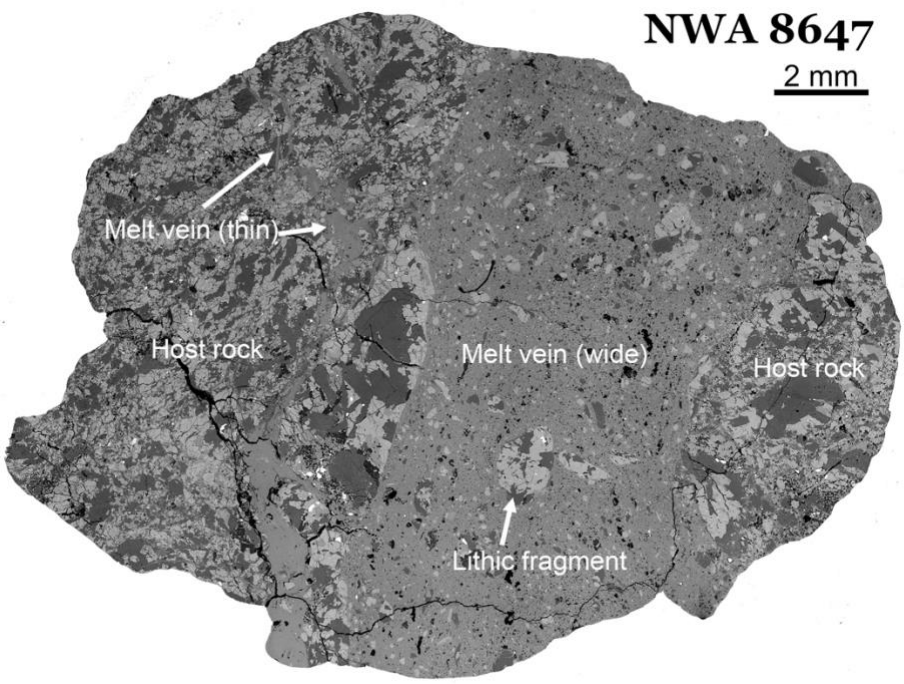

Figure 1. The mosaic backscattered electron image of a polished section of the eucrite Northwest Africa 8647 in this study.

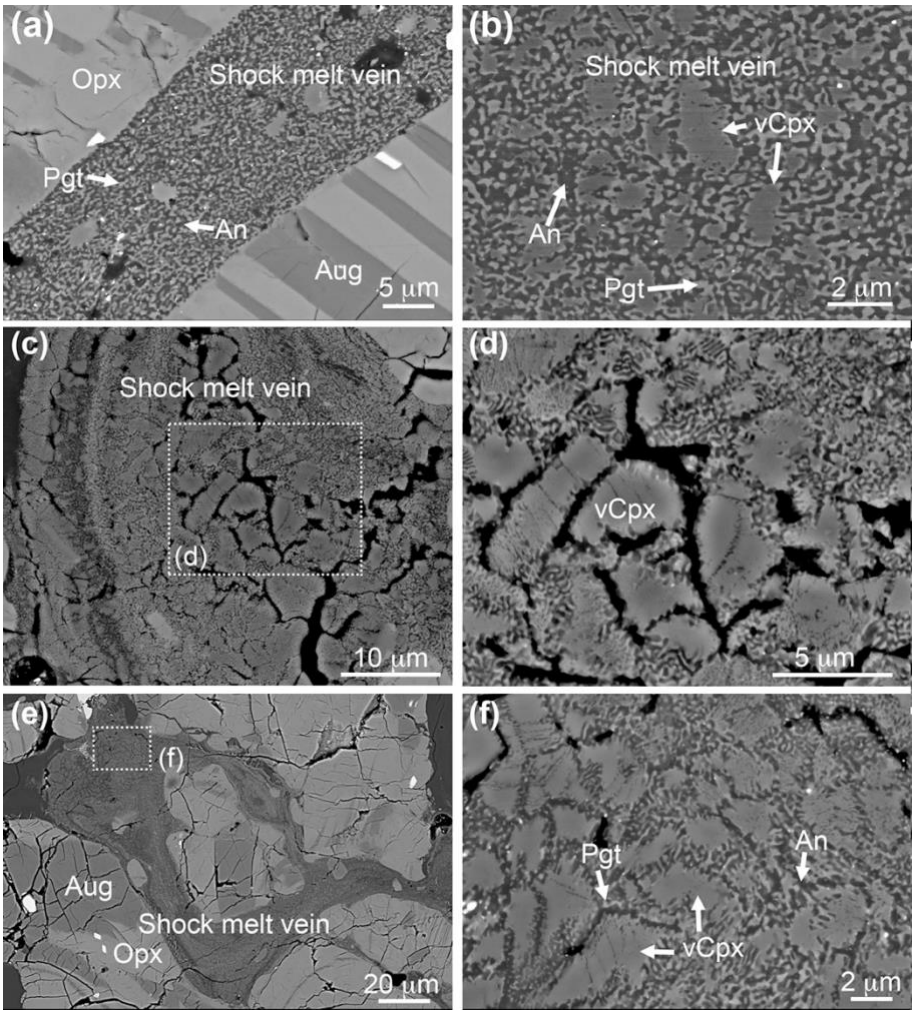

Figure 2. BSE images of typical shock melt veins and the occurrences of vacancy-rich clinopyroxene. (a-b) Typical texture of thin shock melt veins showing that intergranular pigeonite and anorthite with or without irregularly-shaped vacancy-rich clinopyroxene. (c) A thin melt vein containing a very-fine-grained vermicular assemblage of pigeonite and anorthite. Note that in this melt vein relict vacancy-rich clinopyroxene grains mainly occur at the center. (d) The zoom-in image of the rectangle outlined in (c). Fractures are present between different relict vacancy-rich clinopyroxene grains. (e) Another thin melt vein containing vacancy-rich clinopyroxene. In this melt vein, vacancy-rich clinopyroxene is largely retained and vermicular pigeonite and anorthite assemblage occurs along the grain boundary. (f) The zoom-in image of the rectangle outlined in (e). vCpx: vacancy-rich clinopyroxene; Pgt: pigeonite; An: anorthite; Aug: augite; Opx: orthopyroxene.

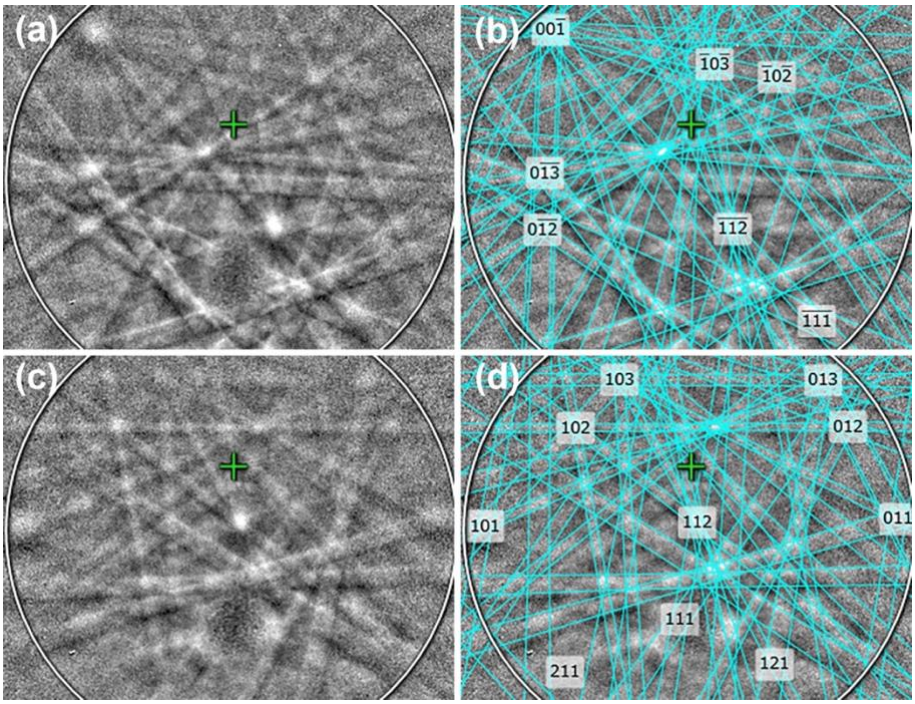

Figure 3. EBSD patterns (a and c) of the vacancy-rich clinopyroxene and the corresponding patterns (b and d) indexed with the C2/c augite structure (MAD=0.53 and 0.38).

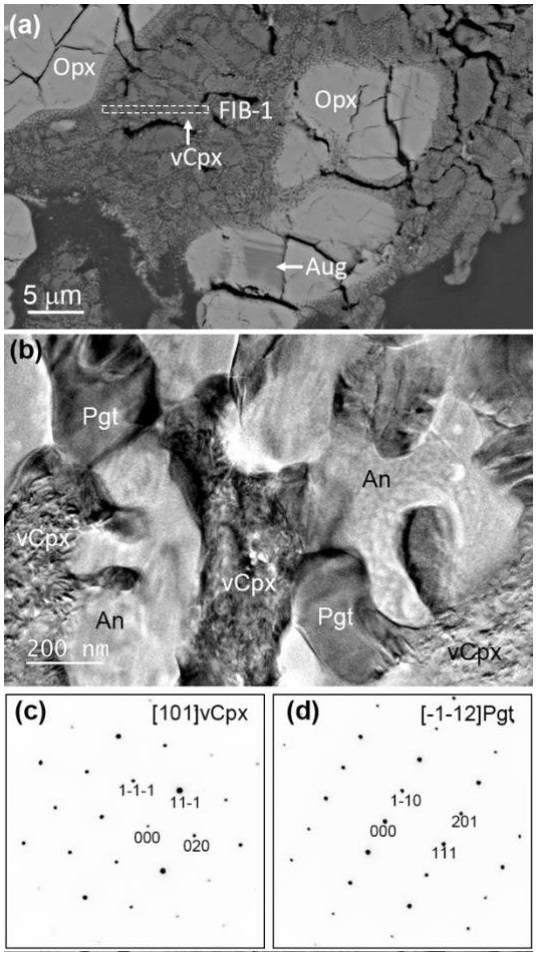

Figure 4. SEM and TEM observations of the vermicular region in NWA 8647. (a) A typical vermicular region with relict vacancy-rich clinopyroxene. The dashed rectangular outline shows the location of a FIB section (FIB-1). (b) Bright field TEM image of a typical area in the decomposition texture. Note the mottled texture in vacancy-rich clinopyroxene, but not in pigeonite. (c-d) SAED patterns of the relict vacancy-rich clinopyroxene and the pigeonite from the decomposition texture. vCpx: vacancy-rich clinopyroxene; Pgt: pigeonite.

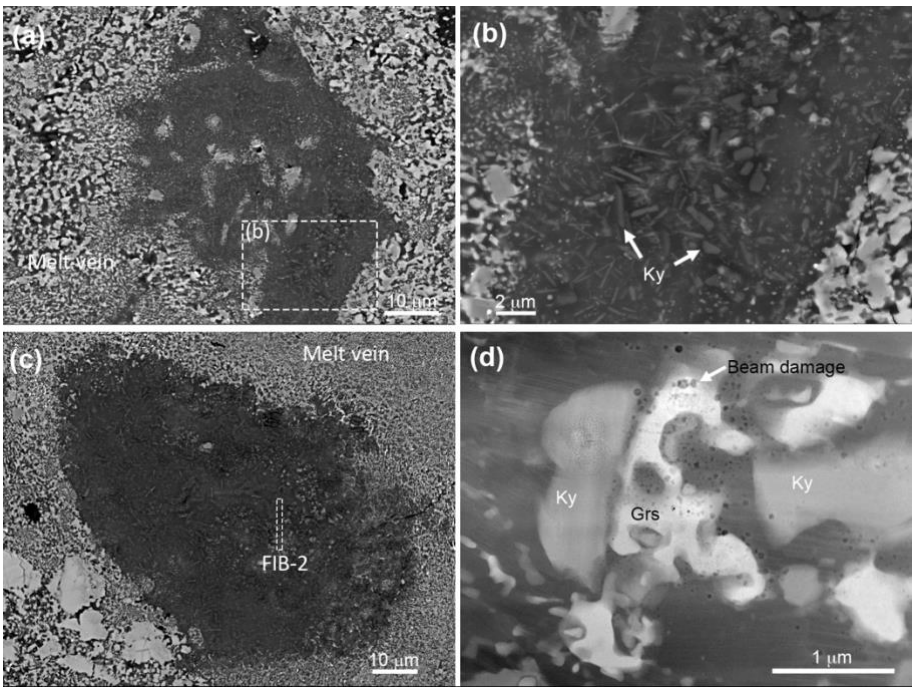

Figure 5. Occurrence of kyanite in NWA 8647. (a) and (c) BSE images of Si,Al,Ca-regions (originally anorthite) in thin melt veins in NWA 8647. Note that the Si,Al,Ca-regions contain many acicular tiny crystals. (b) A zoom-in image of the rectangle outlined in (a). The dashed rectangle in (c) shows the location of FIB-2 section. (d) HAADF-STEM image of kyanite and grossular grains. Ky: kyanite; Grs: grossular.

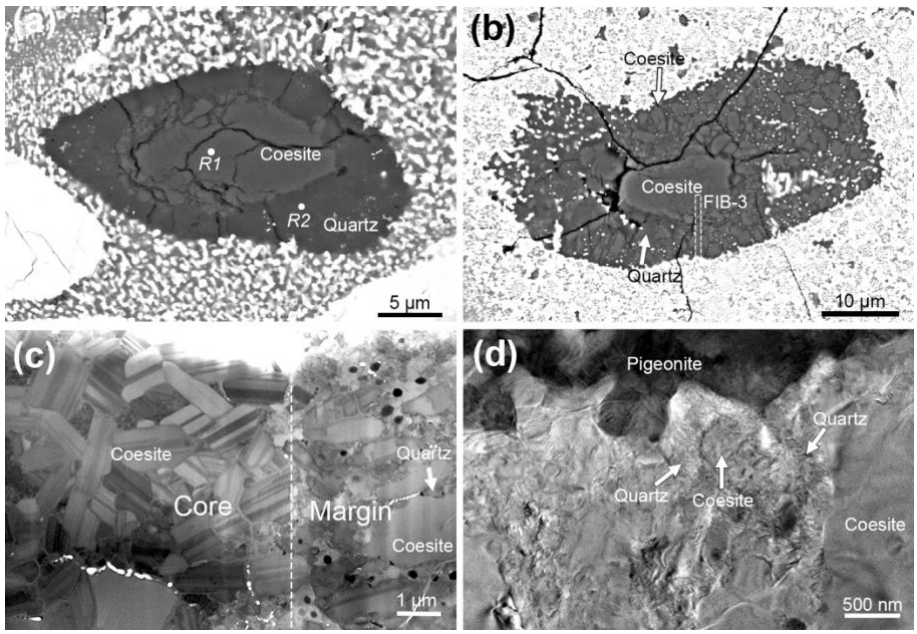

Figure 6. Petrographic texture of the silica fragments entrained in shock melt veins. (a-b) BSE image of typical silica fragments with a core-margin texture. In the fragment shown in (a), the margin is quartz-dominated. The two white spots R1 and R2 indicate the positions of Raman spectroscopic analyses shown in Fig. S11. In the fragment shown in (b), the margin contains small coesite grains and minor quartz grains. A FIB section (FIB-3) was prepared and its location is outlined by the white rectangle. (c) Bright field TEM image of the FIB section containing coesite grains in both the core and the margin. The white dashed line in (c) indicates the interface between the core and the margin. Note the coesite grains at the core show polysynthetic twinning. However, no twinning structure is present in the coesite grains at the margin. (d) Bright field TEM image showing the interface between coesite and quartz.

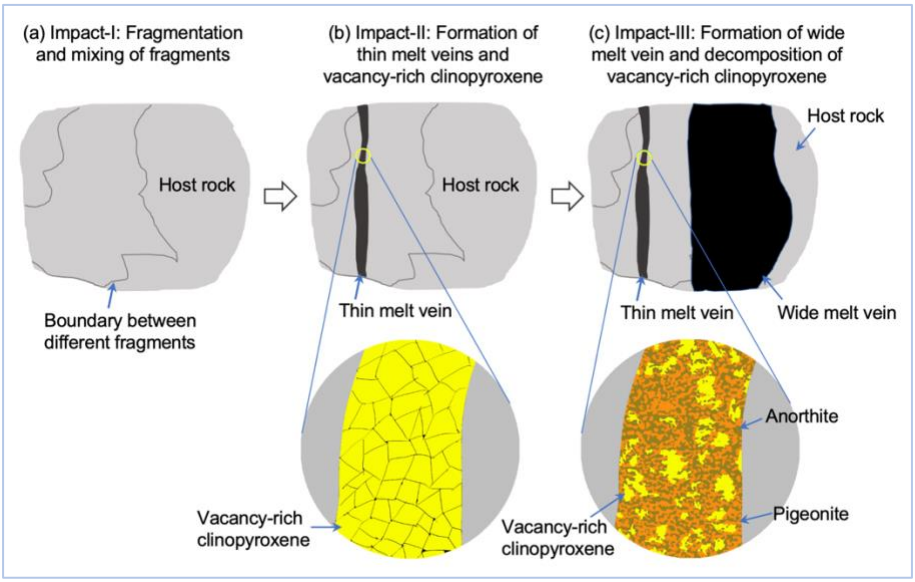

Figure 7. Schematic diagram of the impact history of NWA 8647. During Impact-I (a), the source rock of NWA 8647 was fragmented and different fragments with various grain sizes mixed with each other. During Impact-II (b), vacancy-rich clinopyroxene (shown), as well as twinned coesite and kyanite-grossular (not shown) formed in thin melt veins. During Impact-III (c), vacancy-rich clinopyroxene grains decomposed to anorthite and pigeonite, and coesite grains (not shown) either back-transformed to quartz or lost twin features at their margins.

Table 1. EPMA compositions of vacancy-rich clinopyroxene in NWA 8647

	18	19	20	21	35	43	44
SiO_2	47.42	47.68	48.41	47.66	48.93	48.27	48.19
TiO_2	0.33	0.28	0.24	0.35	0.12	0.15	0.14
Al_2O_3	20.28	18.54	16.32	18.38	17.76	16.42	17.32
Cr_2O_3	0.22	0.16	0.19	0.22	0.12	0.17	0.17
MgO	4.74	5.48	6.38	5.21	6.72	7.07	6.64
FeO	12.96	15.02	16.45	15.71	12.72	15.02	14.44
MnO	0.42	0.52	0.55	0.54	0.48	0.54	0.53
CaO	12.47	11.67	10.80	11.27	12.08	11.00	11.66
Na_2O	0.85	0.75	0.77	0.85	1.12	0.86	0.84
K_2O	0.06	0.07	0.05	0.08	0.05	0.04	0.03
Total	99.75	100.17	100.16	100.27	100.10	99.54	99.96
			Calculated based on 6 oxygen atoms				
Si	1.736	1.754	1.790	1.756	1.783	1.786	1.773
Ti	0.009	0.008	0.007	0.010	0.003	0.004	0.004
Al	0.874	0.802	0.710	0.797	0.761	0.715	0.749
Cr	0.006	0.005	0.005	0.006	0.003	0.005	0.005
Mg	0.260	0.303	0.354	0.288	0.367	0.393	0.366
Fe	0.395	0.460	0.507	0.482	0.386	0.463	0.443
Mn	0.013	0.016	0.017	0.017	0.015	0.017	0.016
Ca	0.489	0.460	0.428	0.445	0.472	0.436	0.460
Na	0.060	0.053	0.055	0.060	0.079	0.061	0.060
K	0.003	0.003	0.002	0.004	0.002	0.002	0.001
Cations	3.846	3.863	3.875	3.865	3.872	3.882	3.877
Vacancy	0.154	0.137	0.125	0.135	0.128	0.118	0.123
Ca-Eskola(%)	30.1	26.8	24.6	26.3	25.3	23.4	24.4

705 Table 2. Defocused-beam EPMA compositions of vermicular and intergranular assemblage of pigeonite and anorthite

	Vermicular assemblages															Intergranular assemblages				
	25	26	27	28	29	34	36	37	38	39	46	47	48	49	57	58	59	60	61	62
SiO_2	48.70	48.47	48.38	47.60	48.32	47.32	47.63	48.19	48.24	48.67	48.97	48.77	49.16	47.91	48.86	45.74	48.62	48.64	48.90	48.56
TiO_2	0.23	0.24	0.27	0.30	0.24	0.19	0.36	0.30	0.34	0.26	0.17	0.14	0.15	0.31	0.52	0.57	0.53	0.57	0.51	0.45
Al_2O_3	14.84	15.27	15.62	18.38	14.83	18.24	17.68	15.39	16.66	14.11	15.00	15.85	14.81	16.63	17.30	19.27	16.70	16.86	16.47	16.30
Cr_2O_3	0.21	0.16	0.17	0.17	0.18	0.13	0.21	0.19	0.18	0.15	0.13	0.12	0.09	0.16	0.26	0.32	0.28	0.31	0.32	0.30
MgO	6.81	6.53	6.61	5.40	6.68	5.23	5.60	6.49	5.85	7.13	7.07	6.76	7.23	6.38	5.61	5.26	5.50	5.66	5.75	5.44
FeO	18.07	17.63	18.21	15.20	18.28	14.12	15.84	17.69	16.52	18.82	17.87	16.17	17.08	16.95	14.71	16.29	15.28	15.03	15.12	15.86
MnO	0.61	0.58	0.61	0.47	0.60	0.53	0.54	0.58	0.54	0.66	0.61	0.58	0.59	0.53	0.46	0.47	0.47	0.48	0.53	0.49
CaO	9.99	10.23	9.94	11.76	9.94	11.99	11.15	10.30	10.74	9.60	10.00	11.10	10.23	10.41	11.69	11.95	11.33	11.72	11.40	11.15
Na_2O	0.79	0.77	0.86	0.81	0.74	0.80	0.83	0.66	0.70	0.65	0.67	0.67	0.77	0.69	0.80	0.44	0.72	0.67	0.78	0.67
K_2O	0.05	0.05	0.07	0.06	0.06	0.06	0.06	0.06	0.05	0.05	0.05	0.05	0.07	0.04	0.05	0.03	0.04	0.04	0.04	0.05
Total	100.2	99.93	100.7	100.1	99.87	98.61	99.90	99.84	99.82	100.1	100.5	100.2	100.1	100.0	100.2	100.3	99.46	99.99	99.81	99.27

706